FEEG3003: Individual Project

A low-cost user operated approach to mapping background radiation in hazardous environments

Thomas Green

This report is submitted in partial fulfilment of the requirements for the Masters of Mechanical Engineering, Faculty of Engineering and the Environment, University of Southampton.

Word Count: 10,062

April 23, 2022

Abstract

A device was conceptualised and built to detect radiation levels from a substantial distance. This device used a Raspberry Pi and additional modules to allow an operator to determine areas of radiological interest, all whilst physical separation was possible. This was enabled by a remote control rover platform housing a georeferencing, radiation detecting sensor unit. The recorded data was then compiled in a comprehensible heat map format, allowing the operator to immediately identify of areas of elevated radiation.

In 95% of instances, the sensor unit was able to accurately determine its current position to within 8 metres. Radiation data collected was found to have precision of ±7.3%, whilst proving to be comparable to that of a commercially available equivalent, with a Spearman's Rank Correlation Coefficient of 0.76. This was achieved at 28% the cost of the commercial offering.

Declaration

I, Thomas Green, declare that this thesis and the work presented in it are my own and has been generated by me as the result of my own original research. I confirm that:

1. This work was done wholly or mainly while in candidature for a degree at this University;
2. Where any part of this thesis has previously been submitted for any other qualification at this University or any other institution, this has been clearly stated;
3. Where I have consulted the published work of others, this is always clearly attributed;
4. Where I have quoted from the work of others, the source is always given. With the exception of such quotations, this thesis is entirely my own work;
5. I have acknowledged all main sources of help;
6. Where the thesis is based on work done by myself jointly with others, I have made clear exactly what was done by others and what I have contributed myself;
7. None of this work has been published before submission;

Acknowledgments

I would like to thanks Professor Simon Cox for his guidance, spirited conversation, and never wavering willingness to help. The project would have been markedly less enjoyable without his weekly meetings.

In addition, I would also like to thank Adam Driver for the provision of remote control parts, without which I would be unable to test my 3D printed component designs.

Also, I would like to thank Amy Kelt for her companionship on tens of hours of data collection expeditions spanning the country.

Finally, I would like to thank Engineering Nonsense for providing the designs of his Tarmo RC car, without which this project would have been untenable.

Nomenclature

List of Abbreviations

CPM Counts Per Minute

CPS Counts Per Second

ESC Electronic Speed Controller

GM Geiger-Müller

GPS Global Positioning System

OSM Open Street Maps

PPE Personal Protective Equipment

PWM Pulse Width Modulation

TPU Thermoplastic polyurethane

Physics Constants

λ Decay constant

N_0 Initial number of nuclei

$t_{\frac{1}{2}}$ Half Life

A Activity

Bq Becquerels

N Number of nuclei

Contents

1 Introduction

Since the mid 20^{th} century the use of nuclear technology has become increasingly widespread. For many years one of its main uses has been power generation in nuclear power reactors. Whilst nuclear power generation has been shown to be one of the safest methods of energy production, with less than $\frac{1}{10}^{\text{th}}$ the number of deaths than gas and coal energy production [1], incidents do still occur and occasionally these incidents go undetected or are concealed from surrounding communities, see the 1986 Chernobyl incident [2] or the 2014 Rössing Uranium Mine incident.

Nuclear incidents are not limited to the breakdown of nuclear power plants; uranium mines, nuclear waste storage and civilian nuclear incidents [3] have also occurred in recent years and gone undetected. There have been incidents involving radioactive material going undetected for long periods of time, due to the lack of visual or olfactory indications of radiation, and the relatively long period of time for health conditions due to exposure to medium-low amounts of radiation to become apparent.

Failing to detect radiation leads to prolonged exposure to radiation for local communities, resulting in avoidable long-term health conditions such as cancer and possible fatalities. Formerly detecting radiation and determining the source of radiation was a dangerous and expensive exercise, mandating expensive equipment, a considerable amount of protective equipment, and risked exposing a large number of personnel to radioactive substances. In recent years the process has become substantially safer through the use of telerobotics.

A telerobot is a robot controlled at a distance by a human operator [4]. They can be fully autonomous, semi-autonomous or exclusively controlled by the operator. Telerobots are routinely used by institution such as NASA and military organisations to operate in hazardous environments where it is unsafe to have a physical presence. The telerobots used by these large companies are highly developed, carrying extremely precise instruments and are priced accordingly, and as such they are out of reach of many consumers.

1.1 Aims and Objectives

1.1.1 Aim

The aim of this project is to design and build an affordable radiation monitoring telerobot. A Raspberry Pi will be used to interface with a Geiger counter module and a controller used to control the telerobot's movement.

1. **To design and build a mobile platform to host sensors**
   The platform is required to be robust enough to traverse difficult terrain whilst taking repeatable data input from the attached sensors. The cost of the sensor components should not exceed £200.

2. **To achieve remote control of the robot using a Raspberry Pi**
   By using the low-cost commonly available Raspberry Pi as the main processing unit the project will be highly accessible to those seeking to replicate the project. The cost for the rover components should not exceed £150.

3. **To use a Geiger counter to measure the levels of ionising radiation in a chosen area**
   The Geiger counter should be able to produce data that has an acceptable level of accuracy and is useful in the real world.

4. **To compile the data from the sensors so that it is easy to interpret**
   The data received from the platform should have the intensity levels of radiation geographically tagged, which allows a heat map of the data to be plotted.

1.2 Design Challenge

This project will have some significant design challenges in regards to the sensor platform and its mobility

1. **Versatility of robot**

   The robot will have to traverse difficult terrain in environments where there is no physical access. As a result the robot needs to be four-wheel drive to avoid getting stranded, furthermore the robot should have a rudimentary object avoidance system to avoid issues occurring due to operator error.

   As the robot will be driven remotely a camera feed will be required from the robot to the operator. For ease of operation of the robot, this feed should have a wide field of view, a low latency, and the input from the controller should be synced with the image relayed from the robot.

   Finally the range of wireless operation should be sufficiently far to allow for the operator to be a safe distance from any potential sources of radiation.

2. **Accuracy of Data**

   All the collected data needs to be accurate and repeatable. It must be ensured that they way in which the Geiger counter is mounted does not have an effect on the radiation readings.

   The expense of a calibrated Geiger counter makes them unobtainable for this project and so direct comparisons can not be made, however, the radiation data collected by the rover should be comparable to data from previous surveys and other publicly available records.

3. **Data Processing**

   The data is to be processed in a way in which it is easy for a layman to understand. This may be achieved using data visualisation, and in particular heat maps to show areas of high intensity and those of low intensity. The initial heat maps may only be indicative of radiation levels, however following further analysis the compilation of more accurate radiation maps should be possible.

2 Background

2.1 Radioactive decay

Radioactive decay is the spontaneous breakdown of an atomic nucleus resulting in the release of energy and matter from the nucleus [5]. This energy release is in the form of radioactive particles and rays, most commonly consisting of alpha particles, beta particles, and gamma rays. These particles and rays have differing energies and so the penetrating ability is affected. Figure 1 sets out the penetrating distance of each of the particles, alpha particles, with the lowest energy, can penetrate the least being stopped by a thin section of paper, whilst very high energy gamma rays are able to penetrate thicker sections of lead.

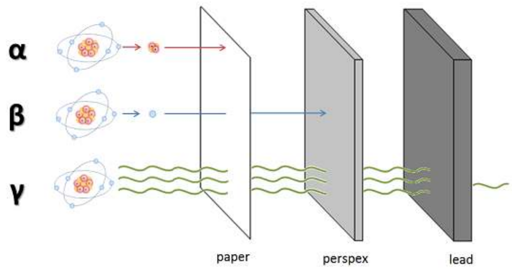

Figure 1: Penetration of radioactive particles and rays [6].

The decay process, and so the radioactivity of the material emitting the energy continues until the nuclei reaches a stable state, that is a state in which the ratio of neutrons to protons is sufficient to no longer require additional energy release. The rate of radioactive decay, or the number of disintegrations of the nucleus per second, is referred to as the radioactive activity and is measured in Becquerels. The activity can be found using the following equation

$$A = \frac{dN}{dt} = \lambda N \tag{1}$$

In the above equation the activity is shown to be a function of N, the number of undecayed nuclei in the substance being measured. Using the following equation and a known initial value of nuclei, the value of N can be formulated:

$$N = N_0 \exp(-\lambda t) \tag{2}$$

A key property of radioactive decay is the longevity of the substance and the time over which it will emit radioactive particles or rays. This can be found using the half-life, the time taken for an isotope's activity to reduce by half, and extrapolating until the isotope has halved sufficiently to no longer give out above background levels of radiation. The equation for half life is as follows:

$$T_{\frac{1}{2}} = \frac{\ln 2}{\lambda} \tag{3}$$

Knowing the half-life is a very useful tool in not only predicting the longevity of a radioactive substance but also deciphering the age of the substance.

2.2 Geiger Counter

A Geiger counter is an instrument that is used to monitor the activity of ionising radiation in the counter's immediate area. The primary component of the counter is a tube filled at a low pressure with an inert gas, called a Geiger-Müller tube. Running through the centre of the GM tube is a positively charged electrode, and the tube itself is negatively charged resulting in a strong electric field.

When a radioactive particle enters the tube it ionises the inert gas molecules causing the the emission of positively charged ions and negatively charged electrons. The electrons, shown in red in Figure 2, are attracted to to the electrode whilst the positive ions, shown in blue, are attracted to the negatively charged tube casing. As the ions and electrons travel through the inert gas they collide with other molecules resulting in further ionisation and the exponential increase we saw in equation 2. This rush of electrons induces a current on the electrode, the magnitude of which determines the levels of radiation in the area.

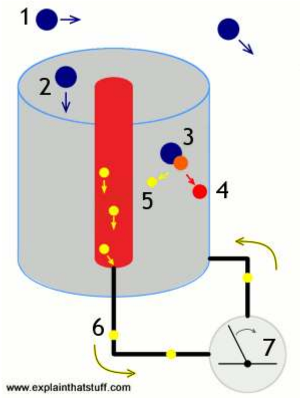

Figure 2: Operation of a Geiger counter [7].

Geiger counters can be used to measure alpha, beta and gamma radiation however they cannot discern between the types of radiation. Many GM tubes have entry barriers or tube walls that are unable to be penetrated by alpha particles and so many cheaper Geiger counters are unable to measure alpha radiation.

2.3 Dangers and effects of exposure to radiation

Ionizing radiation has sufficient energy to affect the atoms in living cells and thereby damage their genetic material [8]. Cells in the body repair the damage caused by radiation however the repair process can often be either unsuccessful, or lead to cancerous cells developing.

Figure 3: Technician suited in PPE measuring radiation [9].

In order to enter areas known or suspected to be radioactive suitable protective equipment, such as a lead apron, a hazmat suit and a gas mask, has to be worn. However this equipment is not effective against high energy, high penetrating ionising radiation [10]. Therefore a physical barrier or sufficient separation is needed between a technician and a highly radioactive area to ensure the safety of the technician. This is achieved through the use of telerobotics.

2.4 Telerobotics

Telerobotics is the human operation of a robot from a distance. It is used in situations where an operator cannot physically enter the environment. Telerobotic systems are split into two distinct sites, the operator site, where the operator will have the controls for the robot and a visual feedback of what the robot is doing, and the remote site, where the operator is unable to access due to hazards in the environment. The remote site is where the robot operates, interacting with the environment in different ways depending the controls input at the operator site. The remote site is separated from the operator site using a barrier and control measures to make the operator site safe.

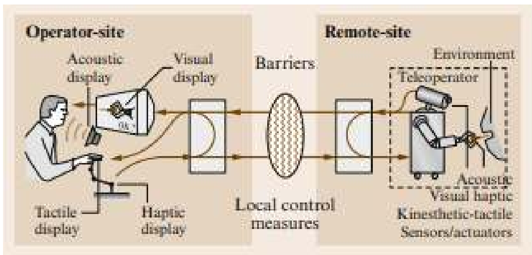

Figure 4: Overview of a telerobotic system [11].

Telerobotics has two main control methods; direct control where the operator has full control over the movement of the robot directly with no automation present; and supervisory control where the operator oversees the operation of the robot but has no real input into the movement and actions of the robot; it is all automated. In between these two levels of control falls shared control in which some degree of automation is present but ultimately the control of the robot is from the operator.

2.5 Geospatial Data Representation

The data received from a sensor is usually limited to attribute information, defining the characteristics of the event that has been sensed, and temporal information, defining the time and period over which an event occured. This data provides useful insight into the nature of an event that has occurred, but fails to incorporate any location information that would facilitate the creation of a map depicting the event.

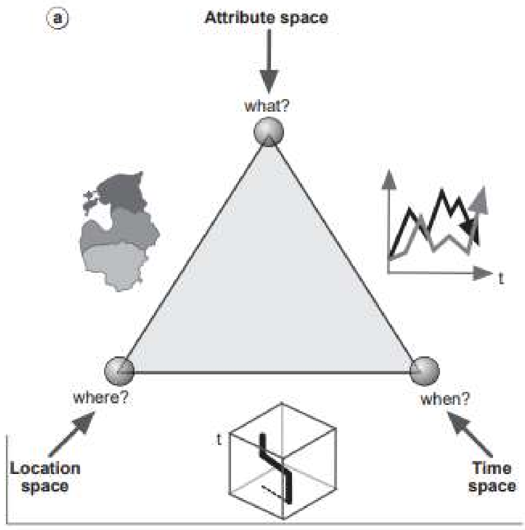

Figure 5: Characteristics of geospatial data [12].

Figure 5 shows the characteristics of the geospatial data, and the visual output that can be created with the corresponding information. The combination of attribute and temporal information allows the production of time-based graphs, attribute and location information allows the production of static maps, and temporal and location information allows the creation of a path timeline plot. A combination of all three elements, with the addition of a cartographic model, allows for the production of detailed maps encompassing information about the location, time, and attributes of events. This visual model can then be used to analyse the events that have occured and using additional geographical information further inferences can be made.

3 Description of Hardware

This section contains a description of the hardware used in the project, as well as the criteria used to determine the suitability of the hardware for the required needs. The following schematic, Figure 6, outlines the arrangement of the hardware with the connections required.

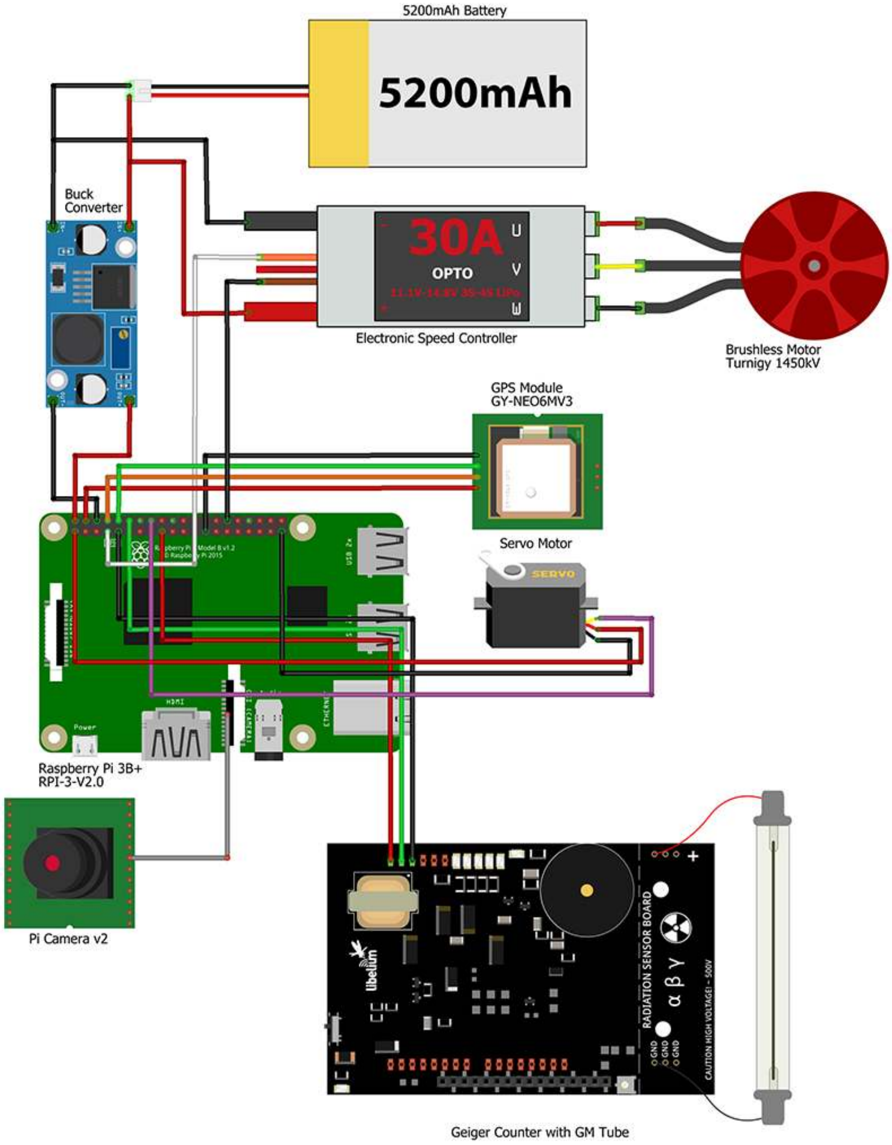

Figure 6: Schematic of the hardware used, connected to a Raspberry Pi. Wire colours were chosen according to the TIA/EIA T568B colour standard.

3.1 Raspberry Pi

The rover interfaces with multiple connected peripherals simultaneously and so a central controller is required. One solution would be to use an array of microprocessors operating in conjunction. However, a single-board computer, such as the Raspberry Pi, provides a more succinct solution. The Raspberry Pi provides wireless interfacing, multiple serial connections, and on board data processing in a compact package.

There have been numerous iterations of the Raspberry Pi, the most recent being the Raspberry Pi 4B and the Pi Zero W. In addition older and less expensive models are still available. Table 1 compares the specification for the available Pi models.

	Pi Zero W	**Pi 3B+**	**Pi 4B**
Price:	£10	£25	£35+
Mass:	9g	45g	46g
Size:	$22.75cm^2$	$47.60cm^2$	$47.60cm^2$
GPIO Pins:	40	40	40
WiFi/Bluetooth:	✓	✓	✓
Clock speed:	1GHz	1.4Ghz	1.5GHz
Processing cores:	1	4	4
Memory:	512MB	1GB	2/4/8GB
Power Supply:	5V/1.2A	5V/2.5A	5V/3A

Table 1: Specification comparison for the currently available models of Raspberry Pi

The major differentiators between the Pi Zero and the other two models are size and price; the Pi Zero being the lower cost, smaller variant. The small footprint of the Pi Zero would allow a more seamless integration into the rover design, whilst the lower power demands would put less strain on the battery. However, the limited processing power was found to be insufficient for the on board data processing required in this project. The Pi 3B+ and the newer revision, the Pi 4B, are similar with the slight differences being a small clock speed improvement and increased memory. During testing, both the Pi 3B+ and the Pi 4B were found to be viable candidates; the Pi 3B+ was selected for the rover due to its lower cost.

3.2 Rover Components

The trade-off between price and performance was a key constraint when choosing components for the rover.

3.2.1 Rover Chassis

The chassis forms an integral part of the rover, acting as a base to attach all the other components, so it is important for it to be a rigid, robust structure. Typical RC chassis are expensive injection moulded products, costing in excess of £100 [13], with limited potential for structural modifications. FDM 3D-printing provides an alternative manufacturing method that allows a greater degree of customisation, at a considerably reduced cost.

There are multiple open-source computer modelled chassis available online. For this project the Tarmo 4 chassis designed by Engineering Nonsense was chosen, primarily due to the integrated four-wheel drive transmission and power train. Whilst the design of the rover was largely based on the Tarmo, modifications were made to mount the sensing equipment, increase the ride height, and allow for greater compatibility for smaller 3D printer beds. Thirty individual 3D printed parts were assembled together using nuts and bolts to form the chassis (Figure 7).

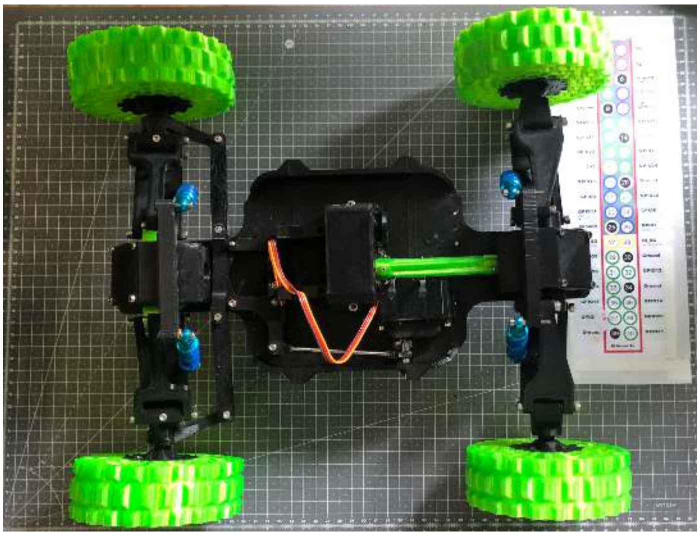

Figure 7: Top down view of the rover chassis. Only the rear wheel drive shaft is connected, the individual parts are secured together using M4 nuts and bolts.

Additional to the chassis there were further components which could feasibly be modelled using CAD and 3D printed instead of being bought, one such component was the track rod ends used in the steering system (Figure 8).

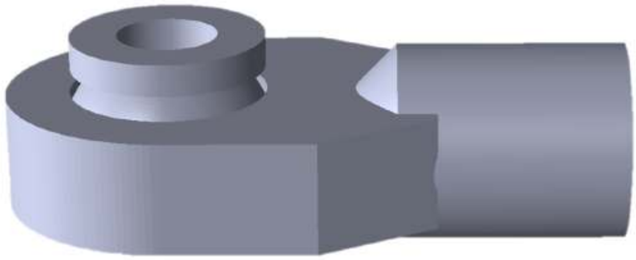

Figure 8: Single piece track rod end designed in Solidworks. Printed at 0.2mm layer height, PLA, 7mm retraction distance, horizontal orientation with raft and minimal supports. The distance between the ball joint and housing is 0.3mm with two connecting spurs which erode away during the first few uses.

3.2.2 Electric Motor and Speed Controller

The rover needed to perform precise, steady, repeatable movements, and this had a large effect on the motor selection process. In addition, the powertrain of the rover had a single gear with a ratio of 0.4:1. This meant that the torque range would be limited by that of the motor, and so a motor with a large torque range was required. The motor chosen was a high-power Turnigy 1450kV; its high performance nature meant it had a large torque range and provided a greater mechanical efficiency at lower speeds, putting less strain on the battery.

To circumvent the need for an expensive transmitter and receiver, the Raspberry Pi was used to control the speed of the motor. This was done by relaying the inputs from a Bluetooth games controller to the Raspberry Pi, which in turn would adjust the motor throttle level, this is explored further in Section 4.1.

During the testing phase, it was found the the high power motor was causing distorsion and eventual failure in the drive shafts. This was particularly apparent during acceleration from a stationary position where torque was at its maximum. To prevent this, software limits were imposed on the maximum throttle (Section 4.2). The drive shafts were also printed in a flexible TPU filament, these would act torque dampeners reducing the destructive vibrations..

3.2.3 Battery

The rover operates as an untethered system, one that requires no physical connections to operate, and so the power source must be integrated onto the rover. This power source is needed to power not only the Raspberry Pi, but also the associated modules and the electric powertrain. The chosen ESC/motor combo requires 11.1 volts to operate, the same as outputted by a 3 Li-Po cells connected in series (3s), whilst the Raspberry Pi requires a 5 volt rail. Since the use of a single battery was preferred for space efficiency, a buck (DC-DC) converter was connected in parallel to the ESC creating two 11 volt paths from the battery. An LM2596 converter then stepped down this voltage to the $5V \pm 10\%$ suitable for the Raspberry Pi.

$$I_{total} = V \left[\frac{R_{RPi} + R_{ESC}}{R_{RPi} \cdot R_{ESC}} \right] \tag{4}$$

$$I_{total} = I_{RPi} + I_{ESC}$$

According to the ESC data sheet the peak continuous current draw is 120 amps, however during experimentation with the powertrain was connected to a bench power supply, it was observed the average current draw was approximately 2.6 amps, peaking at just 20 amps under 75% throttle. This lower than expected current draw meant a smaller battery than previously thought could be used. Including the peak current draw of 2.5 amps from the Raspberry Pi 3B+ [14], and using equation 4, the continuous current draw of the rover was found to be 5.1 amps, rising to approximately 22 amps under heavy throttle. These values can be used to create a battery model to determine the single charge life span of the battery (Figure 9).

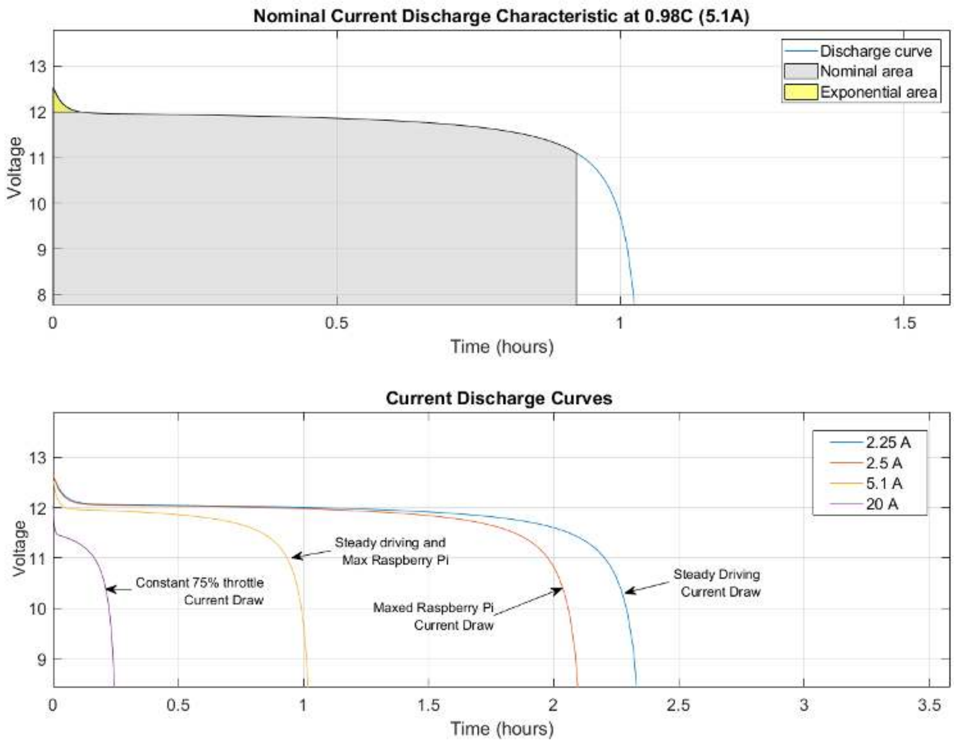

Figure 9: Battery model created using MATLAB Simulink. Four different current draws were highlighted, showing the battery life when the components are performing different functions.

An expectation of the rover was the ability to go on long expeditions, for this it was decided a battery life of one hour would be required. A battery model was created in MATLAB to test various battery life capacities. A 5200 mAh battery was originally found to provide 62 minutes of power when the Raspberry Pi was connected and the rover was being driven at steady speeds. However, due to under-voltage protection the nominal capacity was found to only provide 52 minutes of power. Whilst this was less than the hour target, the additional expense of a higher capacity battery ran counter to the low-cost aim of the project.

3.3 Sensors

3.3.1 Geiger Counter

The MightyOhm Geiger Counter kit was used due to its low expense and multiple interfacing options. The integrated ATtiny2313 microcontroller allowed for serial communication with the Pi whilst being energy efficient enough to be powered directly from the Pi's 3.3V power rail. The Geiger counter came as a kit (Figure 10) requiring soldering and assembly. All connections were checked before inserting the GM tube to ensure no potentially damaging short circuits.

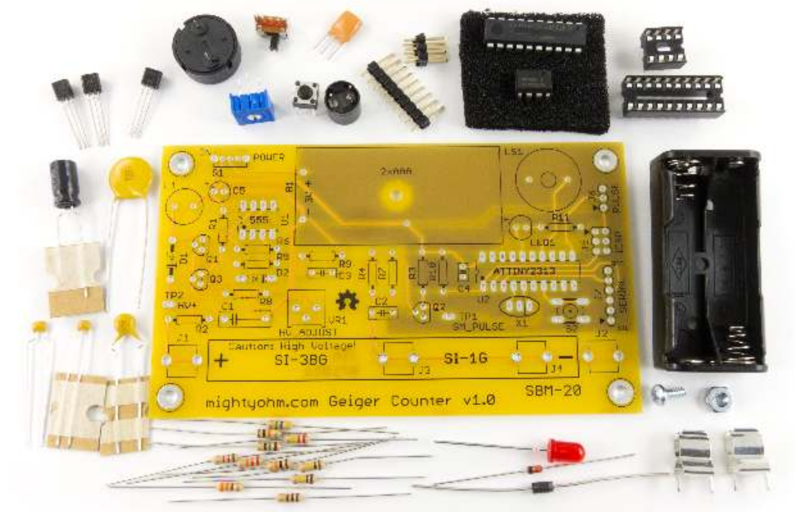

Figure 10: The unassembled MightyOhm Geiger Counter Kit [15].
This image is licensed under CC BY-SA 2.0.

An SBM-20 GM tube was used, this had a moderate Ra^{226} gamma sensitivity of 29 cps/mR/hr [16]. The tube has a stainless steel cathode which also serves as the outer chamber wall, as a result the tube was only sensitive to beta particles and gamma rays.

3.3.2 Camera Module

The camera module used was the Raspberry Pi Camera V1, containing a 5 Megapixel Omnivision OV5647 sensor capable of capturing video at 1080p and 60 fps. In future iterations the Pi Camera V2 would be an improvement given its greater visibility of the surroundings. This was due to the superior 62.20° horizontal field of view (Figure 11) and greater vertical field of view.

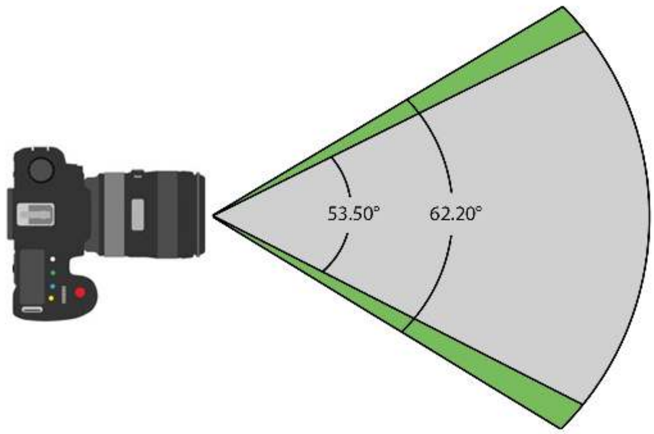

Figure 11: In grey the horizontal field of view of the Pi V1 camera of 53.50°, in green the additional field of view of the Pi V2 camera is highlighted.

3.3.3 GPS

A GPS package of a ublox NEO-6M module combined with a passive ceramic antenna was chosen due to its low cost. The passive antenna provided no signal gain, and so indoor usage of the module resulted in patchy results, however when used outdoors a strong satellite connection was present. The accuracy of the GPS module is assessed in Section 5.1.

4 Rover control

4.1 Motor Control

The servo motor for the steering system and the ESC are both controlled using pulse width modulation (PWM). However, they employ different methods to translate the PWM signal to the appropriate rotation.

4.1.1 Servo motor control

From its neutral position, a servo motor can only rotate 90° in either direction. The magnitude of the rotation is proportional to the width of the electrical pulses sent over the control wire. The servo motor has a pulse width range of 1ms to 2ms, with 1.5ms being the neutral position (Figure 12).

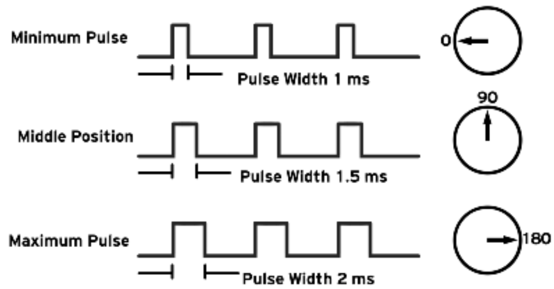

Figure 12: Variable pulse widths and their associated servo positions [17].

4.1.2 Brushless motor control

To control the brushless motor PWM signals are fed into the ESC. These 1 ms - 2 ms pulses are then relayed to the motor. A pulse width of 1ms corresponds to no throttle whilst a width of 2 ms corresponds to full throttle.

Brushless motors require an arming and calibration process at the beginning of every use. This involves certain throttle levels being set in quick succession. By monitoring the transmitter output, the arming sequence was decoded and replicated in python to be performed on command.

4.2 Controller interfacing with motors

For the rover movement, two controller inputs were monitored: the left joystick to control the steering system, and the right trigger to control the throttle. Both the joystick and the trigger are analogue inputs. The trigger position is determined using a hall effect sensor, whilst the joystick position uses two potentiometers.

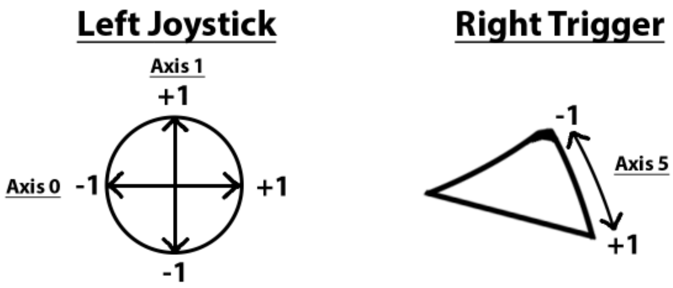

Figure 13: The axes of the joystick and trigger with their associated limits.

Only the position of the joystick on the horizontal axis (Figure 13) was used to manipulate the steering of the rover. The library used conveyed the position of the joystick as a float between -1 and +1. This magnitude of this float was then used to turn the wheels to the desired angle.

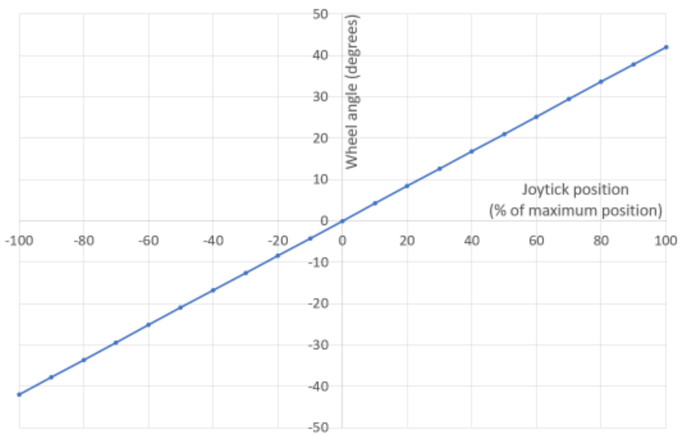

Figure 14: The response curve designed for the left joystick. This is a 1:1 linear mapping of the joystick position to wheel angle, with limits imposed at +42°and -42°.

A linear response curve (Figure 14) was designed so that every increment in the position of the joystick resulted in a constant increment in the wheel angle. A maximum turning angle of 42° was possible before chassis interference. This corresponded to a minimum pulse width of 1.27 ms and a maximum pulse width of 1.73 ms. Software limits were imposed so that the maximum joystick inputs would only yield a turning angle of ±42°.

The trigger is a single axis lever and it's position is also relayed as a float value between -1 and +1. In initial testing the response curve was fully linear, a float of -1 would mean no throttle and a float of +1 would mean full throttle. However, at low throttle (<5%) the brushless motor rotation was in discrete steps which resulted in erratic rover movements. To resolve this issue a dead zone was implemented at low trigger travel distances followed by a jump to 5% throttle. Another issue was encountered at high throttle levels (>60%); the significant torque and resulting vibrations caused the 3D printed bearing housings to crack. In addition, the large torsion on the drive shaft was above the mechanical limit of the 3D printed part, resulting in mechanical failure. Implementing a maximum throttle of 60% sufficed in preventing further breakages. The response curve (Figure 15) was designed to ensure the throttle was within a suitable range.

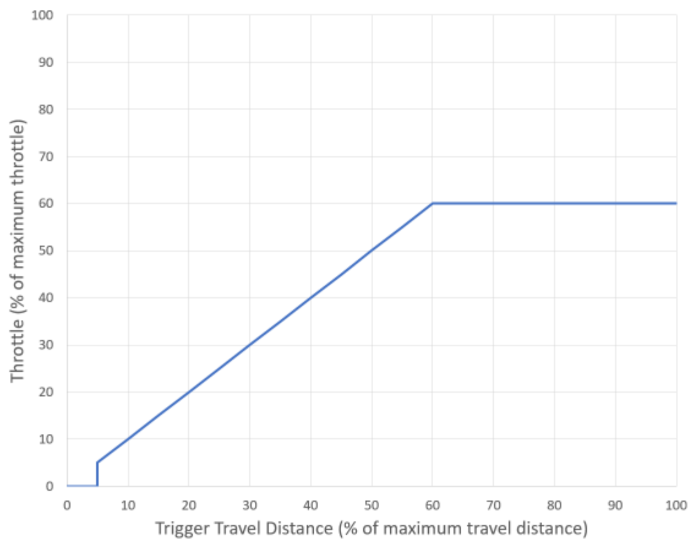

Figure 15: The response curve designed for the right trigger. There is a linear response between 5% and 60% throttle. Above and below these values the aforementioned limits are implemented.

4.3 Controller interfacing with the Raspberry Pi

The controller used contained a class 2 Bluetooth transmitter with a theoretical maximum transmitting distance of 10 metres. During experimentation, it was found that the controller in fact had a range greater than 25 metres (Figure 16). Distances greater than 25 metres caused the signal strength to drop below -80dBm and packet delivery to became inconsistent. This was acceptable for close range control but a greater range would be required to maintain a safe distance from a hazardous area.

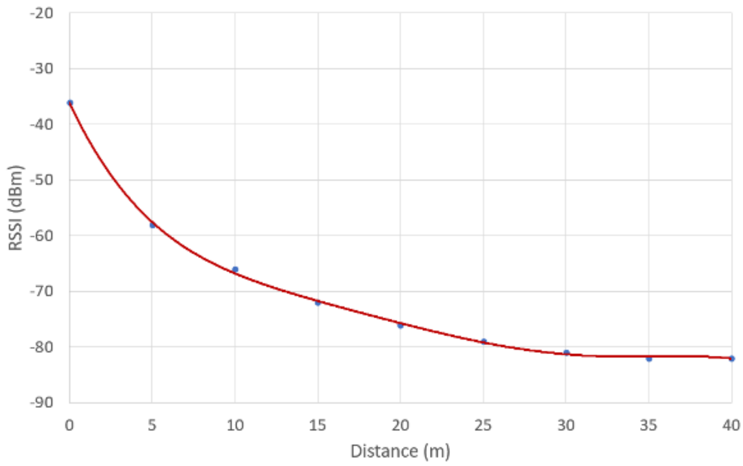

Figure 16: The Received Signal Strength Indicator (RSSI) variation with distance from the games controller. The experiment was performed in an open area with no physical barriers between the detecting computer and the controller.

As discussed in Section 4.4, an 4G hotspot is required for relaying the GUI to the operator. This low latency connection to the operator could also be used to control the rover. The Bluetooth controller was connected to a Raspberry Pi Zero running a program to communicate the controller float values to the Pi 3B+ via the 4G connection. This introduced an additional 62 ms of latency between the control input and the rover, equating to an overall latency of 114 ms. Even so, the rover moved at slow enough speeds that the input latency was found to be negligible.

4.4 GUI

A key aim of the project was to have the rover as accessible as possible. The user interface (UI), as the primary point of contact between the user and the rover, is a significant contributor to the rover's accessibility. Having a largely image based UI, a graphical user interface (GUI), reduces the technological knowledge required to control the rover, and eliminates the need for command-line interactions. A well designed GUI will be able to intuitively be used without the requirement of prior explanation or experience.

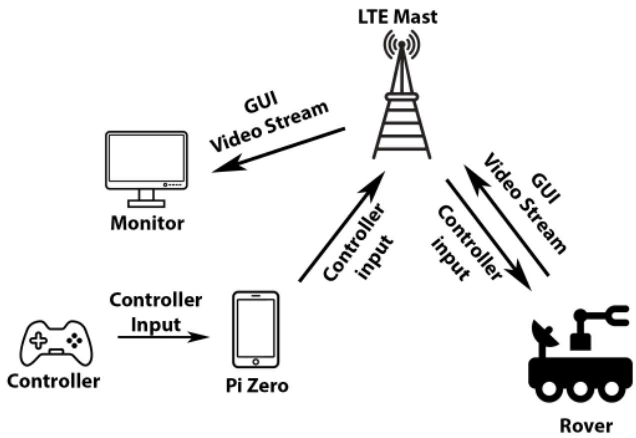

Figure 17: Schematic showing the communication between the operator and the rover when in long range wireless operation using 4G.

The GUI is transmitted to the operator over a mobile network (Figure 17) allowing for long-range control of the robot. Crucially, in order for the operator to have sufficient separation from the hazardous area, a live video stream from the on-board camera was implemented. This facilitated the control of the robot without it being within the operator's sight. A live indication of the current radiation dose rate would also be implemented to allow the operator to plan the subsequent movements. This was integrated using an continuously updating graph on the GUI showing the last 30 seconds of recorded radiation data.

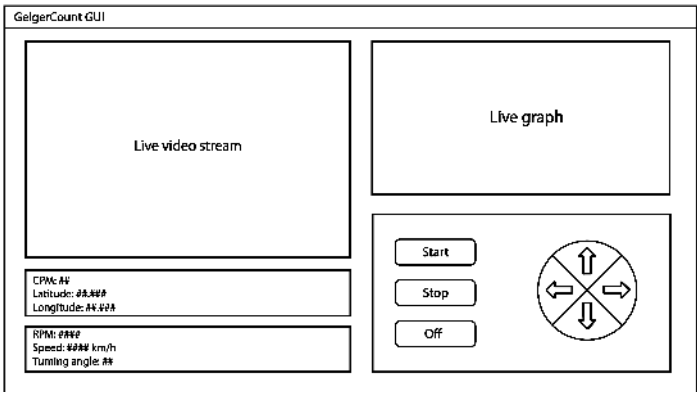

Figure 18: Geiger Counter GUI mock-up showing the placement, size, and arrangement of GUI elements.

A mock-up of the GUI (Figure 18) was created to envision the layout. Most prominence was given to performance critical elements, such as the video stream and live radiation graph. GPS coordinates and details about the current status of the rover, such as speed and wheel angle, were displayed in the bottom left of the GUI. Precision controls for the rover were also included, allowing slight wheel movements to alter the camera direction and navigation along intricate paths. The GUI (Figure 19) created using the tkinter framework. A buffer smoothed the video playback and synchronised the controller inputs with the live video negating the controller input lag.

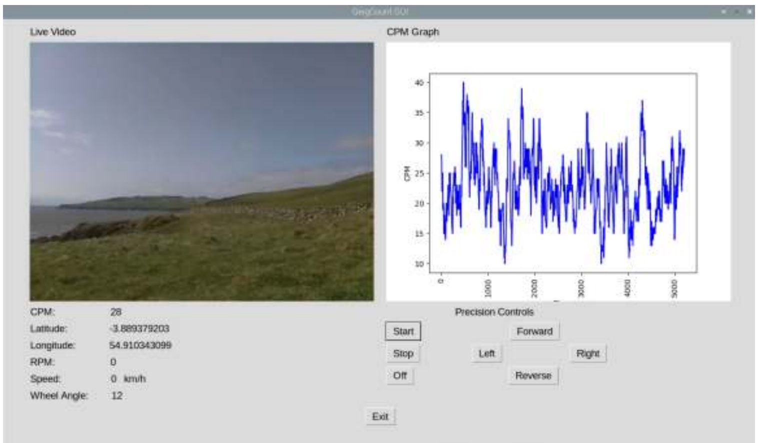

Figure 19: Final GUI created in python using the tkinter framework. The PySimpleGUI package was used to to simplify the code for the element positioning.

5 Mapping and visualisation

5.1 GPS

Serial communication between the GPS module and the Raspberry Pi was via the Pi's primary UART. Packets of data in the form of NMEA messages were continuously transmitted from the GPS module. When the GPS module has a good connection to three or more GPS satellites, these messages will be populated with information about the current position of the module. This position information is generated by considering the time taken for radio waves emitted by the satellites to be received by the GPS antenna. Trilateration is then used to determine the location of the antenna.

Several factors can cause the time taken for the reception of these radio waves to be altered: variations in the atmospheric conditions, obstructions causing additional reflections of the radio waves, and interference with other radio emitters. This causes a reduction in GPS accuracy, particularly with small antenna, low cost passive modules like the one used for this project. With large positional discrepancies, the recorded radiation may be incorrectly geo-referenced leading to inaccurate radiation heat maps.

The accuracy of the GPS module was assessed; it was placed outside on the ground in a built-up urban area near a radio transmitter. This represents some of the more challenging conditions the GPS module may face. The sensor unit was left for 30 minutes, polling the GPS location once every five seconds. From this data, the average latitudinal and longitudinal position of the sensor was found. Haversine's formula (equation 5) was then used to calculate the distance between the true location and each GPS-reported location.

$$\begin{aligned}
a &= sin^2(\frac{\Delta\varphi}{2}) + cos\varphi_1 \cdot cos\varphi_2 \cdot sin^2(\frac{\Delta\lambda}{2}) \\
c &= 2 \cdot atan2(\sqrt{a}, \sqrt{1-a}) \\
d &= R \cdot c
\end{aligned} \tag{5}$$

where:

$\Delta\varphi = \varphi_2 - \varphi_1 =$ Change in longitude

$\Delta\lambda = \lambda_2 - \lambda_1 =$ Change in latitude

$R \quad =$ Radius of Earth

These differences were then plotted (Figure 20) and the proportion of data within the 95% and 60% confidence intervals was found.

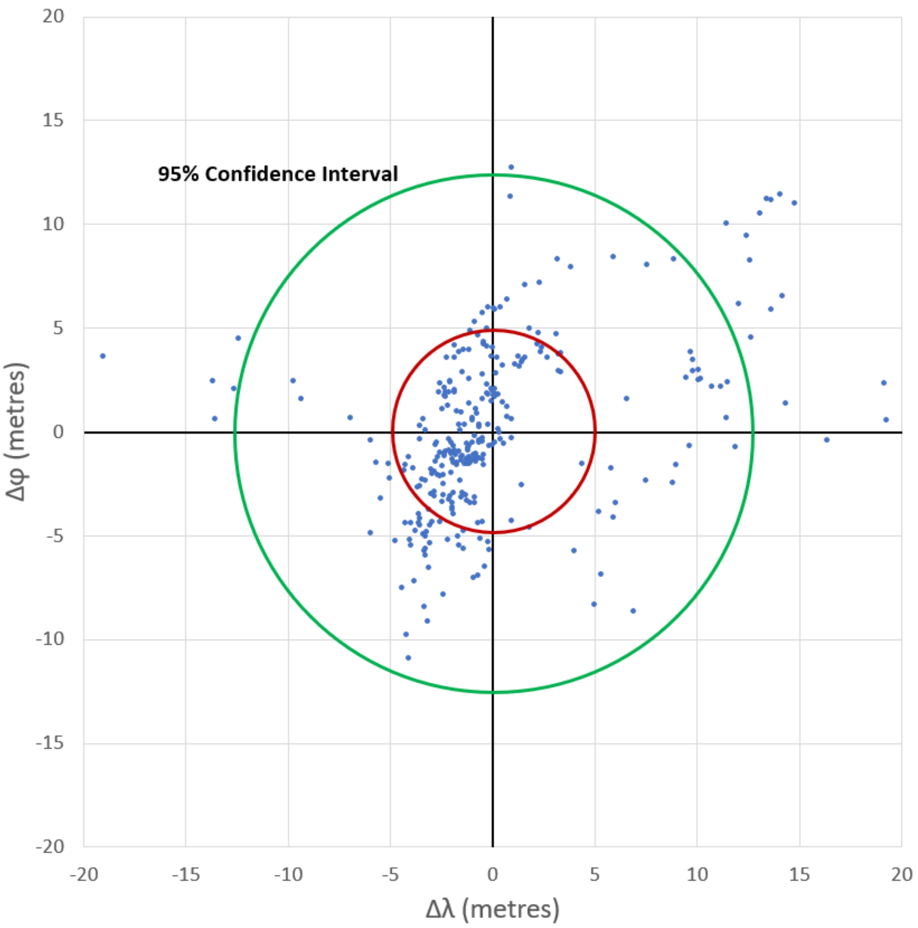

Figure 20: The variance of the latitude and longitude of the GPS when stationary. The green circle indicates the distance within which 95% of the values fall, 12.5m, whilst the red circle is indicative 5m variation from the true coordinates, 62% of values fell within this range. The radius of the earth was taken to be 6372.8 km, and the earth was assumed to be spherical.

As previously mentioned, the experiment represents less than optimal conditions. Even with these conditions, there was found to be a 95% confidence interval of 12.5 metres, whilst over 60% of the values were within 5 metres of the true coordinate. This deviation was deemed acceptable for the aims of this project. When repeating the experiment in an open area, the 95% confidence interval was 8 metres, whilst 60% of values were found to be within 3 metres. With a greater budget available, two GPS modules could be used in conjunction to achieve more accurate differential GPS.

5.2 Geiger Counter

The MightyOhm Geiger counter is a serial device, transmitting data in ten-bit packets at a baud rate of 9600. These packets contained eight data bits, a start bit, and a stop bit. The Raspberry Pi 3B+ only has a single GPIO UART which is already occupied by the GPS module. To allow communication between the Pi and Geiger counter an additional software UART was created. This emulates the functionality of a hardware UART using bit-banging to sample the state of the GPIO pins to which the Geiger counter is connected.

The bit-banging process requires a GPIO pin to be nominated as the RX pin. The RX pin will be monitored for a start bit, and once detected the subsequent data is recorded. If a stop bit is encountered an interrupt is raised. Using bit-banging allows an additional serial device to communicate with the Pi, however the software UART is more prone to errors than the hardware UART. Without correcting for these errors, the decoded serial output was as follows:

```
>> CPS  1   CPM 18  uSv/hr  0.1 SLOW
>> CPS  0   CPM 18  uSv/hr  0.1 SLOW
>> CPS  0   C
>> PM   17  uSv/hr  0.09    SLOW
>> CPS  0   CPM 17  uS
>> v/hr 0.09     "SLOW
>> CPS  1   CPM 18  uSv/hr  0.1 SLOW
```

The output contains numerous errors where the start/stop bits have been incorrectly detected. This causes the strings to be split at improper intervals. As a result the arrays formed from the strings will be incorrectly indexed. An error correction algorithm (Figure 21) was developed to ensure the desired array element was both valid and within the expected range. If this was not the case, a previous value for the array element was used.

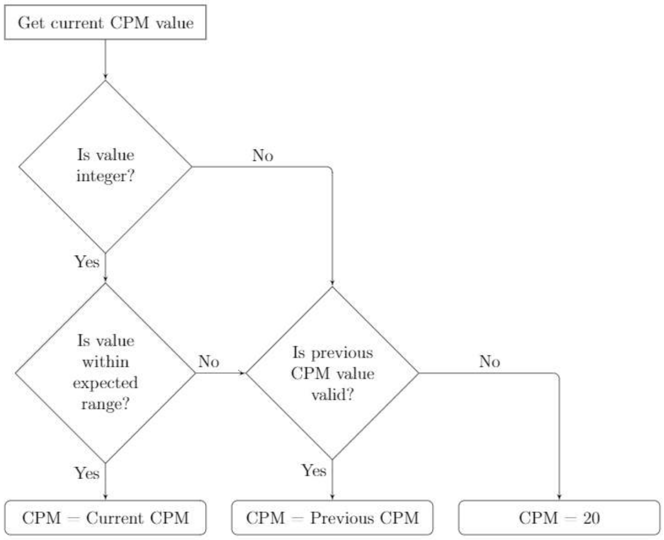

Figure 21: Flow chart of error correction algorithm used to rectify the recorded CPM values when errors occur during the bit-banging process.

The Geiger counter has three selectable operating modes: slow, fast, and instantaneous. Both the slow and fast mode use a sample buffer to average the collected values over a set time, whereas the instantaneous mode bypasses this buffer. The lack of averaging in instantaneous mode led to a noisier signal, causing issues at low sample rates. Both the fast and instantaneous mode yielded similar results (Figure 22 and 23), but the greater noise in instantaneous mode obscured the trendline.

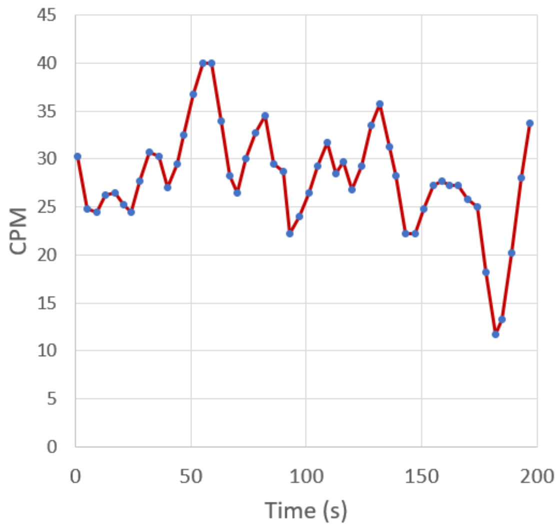

Figure 22: CPM over time when in fast mode

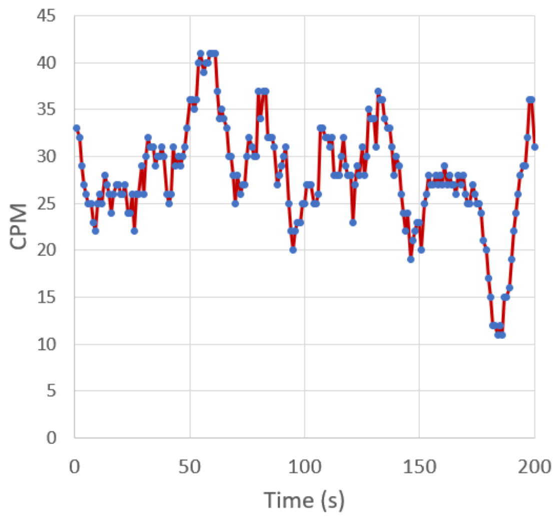

Figure 23: CPM over time when in instantaneous mode

The fast mode was used to avoid the under-sampling and noise issues that occur in instantaneous mode. The GPS module was polled at the same 0.25Hz rate as the Geiger counter. Over this four second period the latitudes and longitudes were averaged to ensure each CPM value was correctly geo-referenced.

5.3 Time Series Graphs

Time series graphs (Figure 24) serve to visualise trends in the data over time. When the data is only in numeric form it is hard to discern any patterns. Once a time series graph has been plotted trends become more obvious. This is very useful when monitoring how data values vary with an external stimuli, such as the experiment outlined in section 6.1.

Time series graphs are most useful when only the temporal and attribute characteristics are being considered. For the purpose of this project, it was also desirable to plot a third characteristic: the location of the rover.

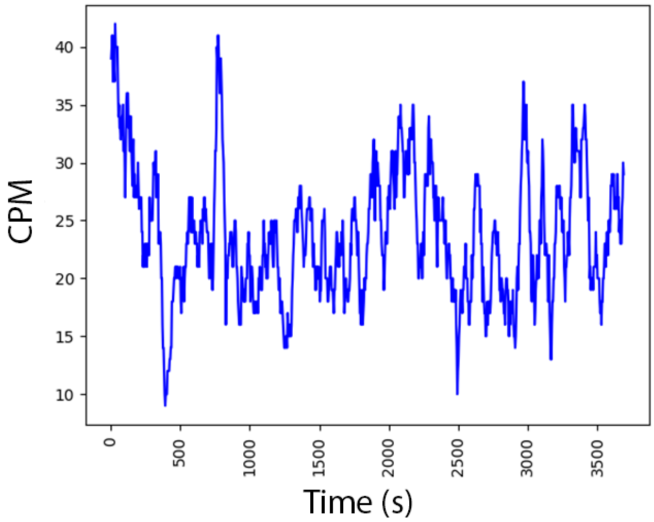

Figure 24: A time series plot of recorded radiation data.

5.4 Geographic Plots

Location data from the GPS module was recorded every time a radiation reading was taken. Compiling this data together creates a location history of the route taken by the sensor unit. As the location is recorded in decimal degrees, a two dimensional graph of the location history can be plotted (Figure 25).

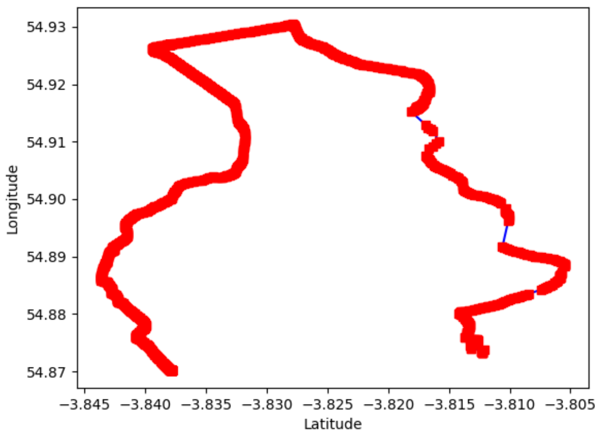

Figure 25: All the GPS locations at which a radiation readings were taken plotted as a scatter graph with latitude and longitude axis.

Whilst this data now has a geographical attribute it is not displayed visually. Instead to find the location of a radiation value the time series data has to be cross referenced with the location data, and so interpreting the combined data is troublesome. To make the data easy to interpret the location, attribute, and temporal data should all be plotted in a single graph. One solution to this would be to use a three dimensional graph. This would show the magnitude of the recorded radiation dose rate as well as the position at which that data was recorded. However, when a large amount of data was collected occlusion issues arose. An alternative method would be to vary the colour and intensity of each geographic data point in conjunction with the radiation level recorded, creating a heat map visualisation.

5.5 Generating Heat maps

Heat maps visualisations are easy to interpret, a key aim of this project. At a glance the operator can see areas of greater radiation which may warrant further investigation. Heat maps also show the trends in the data allowing inferences to be drawn about how radiation varies in differing conditions.

The following algorithm was designed to create the heat maps. The algorithm first rasterises the location data. Radiation data is then assigned to each of these location points. A moving point average was used to minimise the effect of noise on the appearance of the heat map without obscuring data trends.

Algorithm : Creating heat map

Step 1: Read CSV file line by line to create three arrays containing latitude, longitude, and CPM data.

Step 2: Create a zipped list of these arrays to ensure that for each coordinate the correct CPM values is referenced.

Step 3: Create two arrays of defined number of values between the minimum latitude and longitude.

Step 4: Combine the two arrays to create a square matrix of possible latitude and longitudes.
Step 5: Compare every matrix lat/lon value to that of the zipped list, if the difference between the values is within a set threshold assign the zipped CPM value to that matrix position. If the matrix value does not fall in the threshold range assign the CPM as '0'.
Step 6: Create a plot and assign a colourmap so that the CPM values have a different colour. All '0' values are to be set white.

The matrix of latitude and longitude values has to be ordered differently for each hemisphere. The following matrix is the order required for the north and western hemispheres.

$$\begin{bmatrix} lat_{max}, lon_{min} & \cdots & lat_{max}, lon_{max} \\ \vdots & \ddots & \vdots \\ lat_{min}, lon_{min} & \cdots & lat_{min}, lon_{max} \end{bmatrix}$$

The algorithm iterated through the matrix assigning each matching coordinates with the corresponding CPM from the zipped list. This is shown on the following matrix:

$$\begin{bmatrix} 0 & 0 & 34 & 36 & 35 & 32 & 0 & 0 & 0 & 0 \\ 0 & 0 & 0 & 33 & 0 & 0 & 30 & 0 & 0 & 0 \\ 0 & 0 & 0 & 30 & 0 & 0 & 29 & 30 & 0 & 0 \\ 0 & 0 & 29 & 0 & 0 & 0 & 0 & 31 & 27 & 0 \\ 0 & 0 & 28 & 0 & 0 & 0 & 0 & 28 & 29 & 0 \\ 0 & 23 & 0 & 0 & 0 & 0 & 0 & 0 & 26 & 0 \\ 0 & 21 & 0 & 0 & 0 & 0 & 0 & 0 & 0 & 0 \\ 13 & 0 & 0 & 0 & 0 & 0 & 0 & 22 & 23 & 0 \\ 12 & 0 & 0 & 0 & 0 & 0 & 19 & 22 & 21 & 0 \\ 0 & 10 & 0 & 0 & 0 & 0 & 17 & 20 & 0 & 0 \end{bmatrix}$$

This matrix was then plotted using 'imshow' (Figure 27). This was compared to a heat map created using the 'mplleaflet' library (Figure 26).

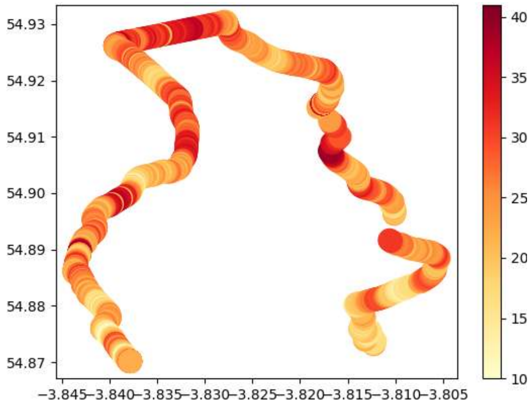

Figure 26: Each individual point is given a colour dependant on its CPM level. There is occlusion due to the many overlapping points, and variations due to noise.

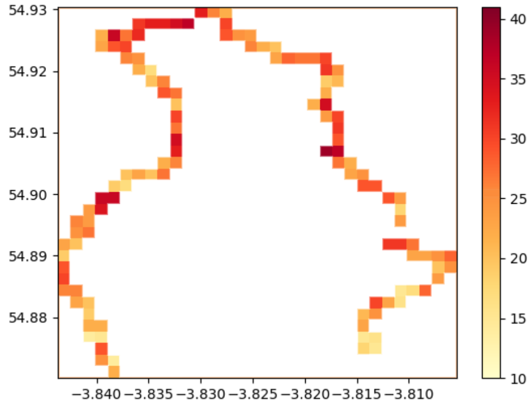

Figure 27: The heat map generation algorithm is used. The trend is still visible but noise has been reduced. Due to rasterisation there is a pixellated appearance.

The intent of the heat map is to give the operator visual indications to the areas in which radiation was greater or lower than normal. As such the interpretability of the initial heat map was prioritised over the accuracy. During the rasterisation process the spatial resolution was reduced, each pixel represented a $3m^2$ area. This reduced the interpretability of the heat maps. To counter this interpolation was used to smooth the transitions from one data point to another. A range of interpolation methods were tested to decide which best represented the data (Figure 28).

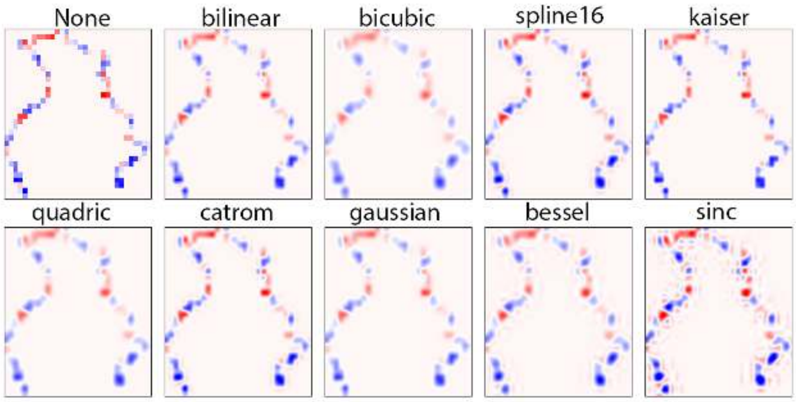

Figure 28: Ten identical coordinate plots created using the diverging colourmap 'bwr', and post-processed using a selection of interpolation methods available from the matplotlib library.

Bicubic interpolation was chosen as it was found to produce the comprehensible heat maps. Once an area of interest had been identified and more extensive data collection had been done, a less rigorous interpolation method was used to preserve the accuracy of the data.

So far the geospatial data has lacked any context. Without context it is hard to determine what could be causing different radiation dose rates, or where exactly areas of elevated radiation are. By adding a topographic base map more can be understood about the locations of these areas.

5.6 Adding a basemap

The following algorithm was developed to fetch the desired topographic base map in a '.png' format. The image file would then be used as a base image for the plot to be overlaid. In order for the base map to be visible all values previously assigned '0' were set to a opacity of 10%. This created a mask of the radiation values which could be displayed on top of the basemap.

Algorithm : Adding base map

Step 1: Convert the heat map to a mask by assigning all white values an opacity of 10%.

Step 2: Find the maximum and minimum longitude and latitude values to create a bounding box area.

Step 3: Using the openstreetmaps API fetch the map encased in the bounding box.

Step 4: Set the fetched map as the plot background.

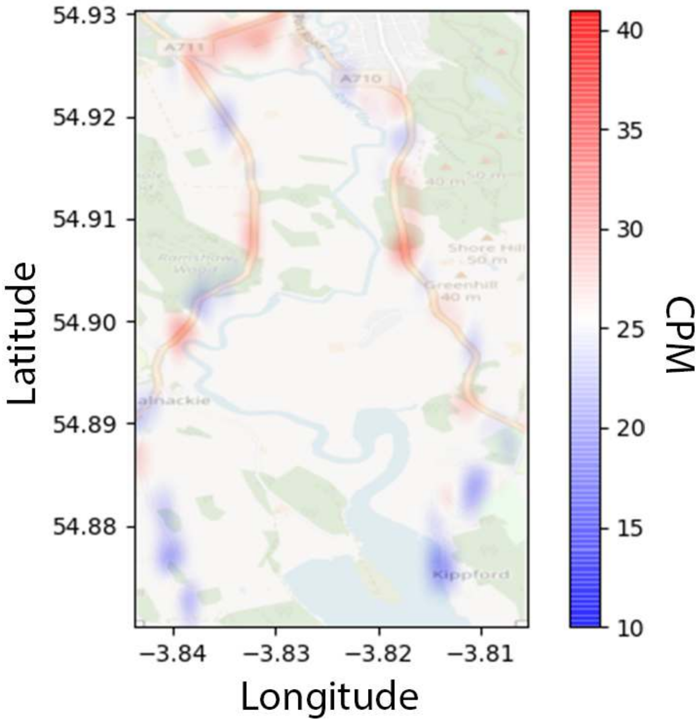

Figure 29: A heat map overlaid on a base map. A diverging colour map was used to highlight areas of radiation above and below what is expected.

The Open Street Maps (OSM) API was utilised due to its open database license allowing free use. OSM uses the WGS84 coordinate system, matching that of the decimal degrees from the GPS module. This allowed the collected latitude and longitudes to be plotted without needing conversion to an alternative coordinate system. In earlier testing Ordinance Survey maps were used, these were based on the OSTN02 coordinate system and resulted in discrepancies between the plotted positions and where they seemed to appear on the base map. The finalised maps using the OSM API (Figure 29) did not suffer from these issues.

6 Operational Acceptance Testing

The following experiments were performed to assess the functionality of the sensor unit (Section 6.1) and to understand how the proximity of certain radiation sources would affect readings (Section 6.2). The rover was then deployed at a decommissioned power station (Section 6.3), these results were compared to previous radiological studies and readings from an open dataset of background radiation measurements.

6.1 Measurements in the proximity of a ionisation-type smoke detector

6.1.1 Experiment Preface

The most common smoke detector type found in domestic settings utilises ionisation chambers to detect the presence of smoke. This is achieved using a small source of an alpha emitting substance, the emitted alpha particles will be impeded by the presence of smoke. This will result in a fall in the alpha particles detected, causing the control circuit to sound the alarm.

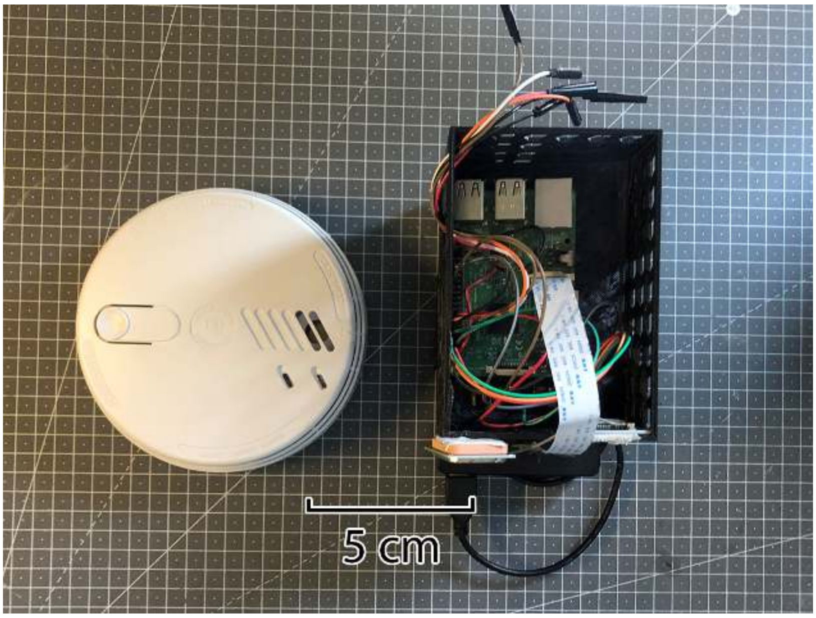

Figure 30: The placement of the sensor unit relative to the smoke detector. The GM tube is on the bottom layer of the storage caddie also containing the other sensor components.

In this experiment the GM tube was placed 5 centimetres from the smoke detector (Figure 30) for 60 seconds before being removed. The ionisation rate was recorded throughout the placement and removal of the smoke detector.

6.1.2 Experiment Hypothesis

The smoke detector used contained one micro curie (1.0μCi) of Americium-241, a primarily alpha emitting radioactive isotope, contained within a capsule. Alpha particles have poor penetrating abilities, with a mean penetration of about 1 cm in air [18]. Therefore a 5 cm air gap would have a significant reducing effect on the alpha particles progression to the GM tube [19]. Furthermore, the GM tube was made of stainless steel further prohibiting the penetration of the alpha particles and so it was hypothesised that the detected ionisation rate would be unaffected by the presence of the smoke detector.

6.1.3 Experiment Results

The detected ionisation rate was plotted on a time-series graph (Figure 31), additionally a six point moving average was plotted to highlight the trend.

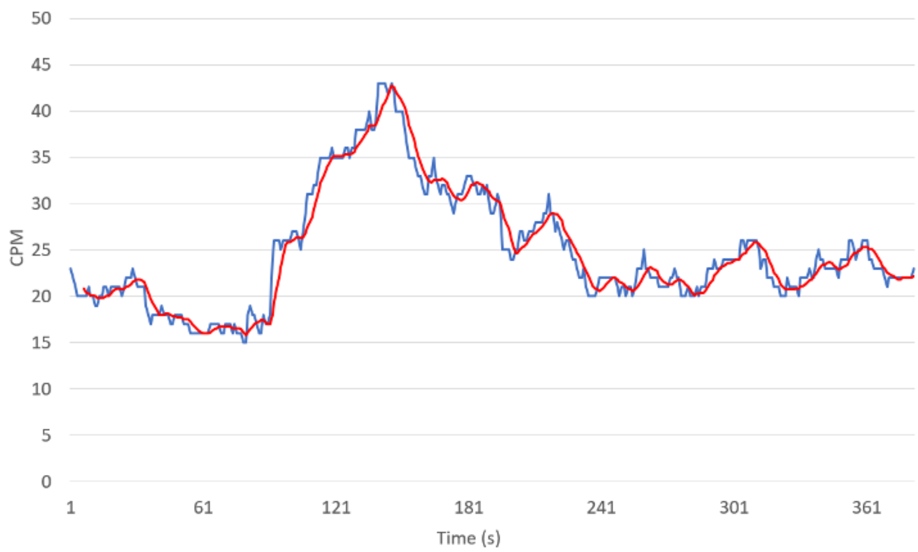

Figure 31: CPM recorded over a period of 6 minutes. The red line represents the moving average over a period of six data points.

6.1.4 Results Discussion

Previous to the introduction of the smoke detector the steady ionisation rate was 18 CPM, when the smoke detector was removed a peak rate of 42 CPM was observed. This represented an increase of 133%. These results contradict the hypothesised outcome, further analysis of the decay of Americium-241 revealed the reasons for this contradiction.

$$\begin{aligned} &{}^{241}\text{Am} \rightarrow {}^{237}\text{Np} + {}^{4}_{2}\alpha \\ &{}^{241}\text{Am} \rightarrow {}^{237}\text{Np} + {}^{4}_{2}\alpha + {}^{59.5\text{keV}}\gamma \qquad (35.7\%) \end{aligned} \tag{6}$$

The usual products during the decay of Americium-241 are Neptunium-237 and alpha particles, however 35.7% of the time low energy gamma rays will also be emitted. These are what is being detected by the sensor unit.

The observed response verified the functionality of the Geiger counter, but fails to shed light on the precision or accuracy of the counter. To gauge the precision the experiment was repeated four subsequent times and the following results were obtained.

Experiment	**CPM rise**	**Absolute Deviation**
1	133%	1%
2	149%	17%
3	126%	6%
4	114%	18%
5	138%	6%

This gave a mean increase of 132% and a mean deviation of 9.6%. From this the precision of the counter was found to be ±7.3%, indicating that the counter was able to produce repeatable, comparable results.

6.2 Variation of radiation over small distances from a concrete mass

6.2.1 Experiment Preface

A significant proportion of background radiation arises due to terrestrial radiation, this is radiation materialising due to the presence of naturally-occurring radioactive elements; uranium, thorium, and radium in rocks and soils [20]. During the production of many building materials, soils and rocks are consolidated and so there is potential for large masses of building materials to contain many radionuclides.

If the Geiger counter were to be positioned near a large mass of concrete, the activity rate derived from the decay of the uranium, thorium, and radium could have a discernible effect on the number of ionisation events detected. This is of particular issue when the Geiger counter is mounted to the rover, where the clearance between the ground and the sensor can range from 100 to 400 millimetres depending on mounting position. There may be a material difference between the the activity levels measured due to radiation originating from a concrete area between the different clearances.

Figure 32: An image depicting the experiment set-up, not to scale. The sensor unit was contained within the bag and attached to the rope. The rope was reeled in a metre at set intervals and held in place. The branch was 5.6 metres high.

This experiment (Figure 32) was designed to explore the effect of increasing the distance between the Geiger counter and a large built-up area of concrete, in this case a large paved patio. The Geiger counter was placed in a plastic bag of 0.5 millimetres thickness. The three common radioactive elements found in building materials decay by emitting alpha particles, undetectable with our equipment, and beta particles [21] which would be impeded by a thicker section of plastic. The plastic bag was attached to an elevated pulley system and raised by one metre at approximately 50 minute intervals until a height of 5 metres was reached.

6.2.2 Experiment Hypothesis

It is evident through the wide use of concrete in construction that it is not a large emitter of radiation, this is confirmed by numerous studies placing the activity concentration of concrete mixes [22] in line with that of water [23] at 18 $Bq \cdot kg^{-1}$. At low masses the concrete should have no perceivable effect on the detected activity level, however concrete has an approximate density of 2000 $kg \cdot m^{-3}$. The patio area was 15 square metres with foundations 15 centimetres deep, and so 4.5 tonnes of concrete was present, it was theorised that this mass of concrete may have a tangible effect on recorded activity levels.

Previous to the experiment it was predicted that the recorded ionisations per minute at ground level would be greatest, then as the sensor was raised the detected rate would fall off. It was proposed that this decline would be most rapid over the first metre of elevation gain and then level off above 1 metre. This hypothesis was reached due to the limited penetrating abilities of beta particles only allowing under one metre of penetration [24].

6.2.3 Experiment Results

The results were plotted as a time series graph (Figure 33). The intervals at which the elevation changes occured are indicated in green, an eight point moving average in red, and the linear regression in black.

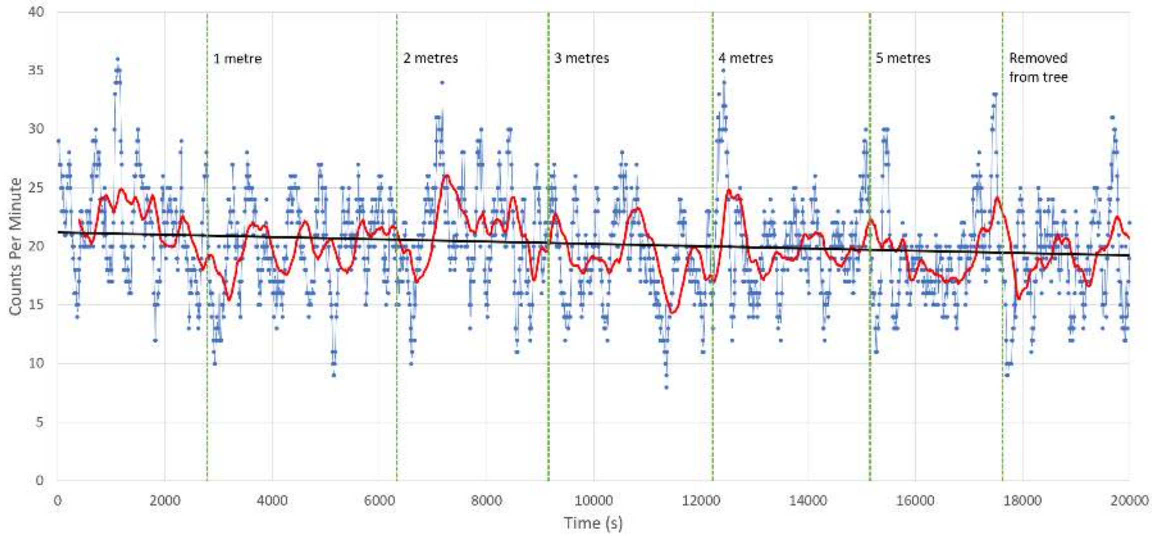

Figure 33: CPM plotted against time, over 6 hours. The black line is the linear regression of the CPM over time. The red line is the moving average of the CPM over 8 data points. In green the times at which the elevation of the sensor changes is indicated.

6.2.4 Results Discussion

When analysing the results the Pearson's correlation coefficient was found to be -0.12, indicating a negative correlation with very weak association. The weakness of the association means that it would be disingenuous to draw any conclusions directly from the linear regression. The ionisation rate remained broadly constant throughout the 6 hour experiment, all data points fall within the range seen during stationary experiments with no additional radiation sources. This indicates that the concrete is not as strong a source of radiation as first assumed, in addition other sources of background radiation will cause more significant changes in ionisation rate than any changes due to the close proximity to concrete.

The results showed that the placement of the Geiger counter on the rover would have no meaningful effect on the recorded ionisation rate, especially over the 100 - 400 mm mounting position range. An additional experiment was performed testing the ionisation rate response to four potential mounting positions on the rover.

Mounting height	CPM range	Average CPM
100 mm	9 - 32	21
200 mm	12 - 31	21
300 mm	7 - 36	22
400 mm	11 - 34	20

For this small range of mounting position the average CPM (over 24 hours) remained consistent at 21 ± 1. This corroborated the previous results and so the recorded ionisation rate was found to be independent from the mounting position of the Geiger counter.

6.3 Mapping radiation levels in the proximity of a decommissioned nuclear power station

6.3.1 Experiment Preface

Chapelcross power station was one of the earliest in the United Kingdom, set-up in 1959 during the Cold War with the purpose not only to produce electricity but also plutonium-239 for use in nuclear weapons. This was achieved using Magnox reactors running on natural uranium, largely composed of uranium-238 with small amounts of uranium-235. The uranium-235 underwent fission ultimately producing electricity, whilst the bulk of the natural uranium, uranium-238, decayed to produce the plutonium-239 sought. The plant operated for 45 years until decommissioning work started in 2004 and is expected to go on until at least 2095.

The location of the station, situated near the town of Annan, was chosen to minimise the radiological effects in the event of a major accident [25]. This meant choosing an area with low population density and in close proximity to a large body of water for emergency cooling. Due to the isolation of the station, the time efficiency of the clean up process has less importance, this has resulted in the Chapelcross site housing the last radioactive waste pond in Scotland [26].

6.3.2 Experiment Hypothesis

In 2003, whilst the station was still active, the average yearly exposure dose of a worker was at 1.37 mSv [27], many times greater than other nuclear power stations. This was common across Magnox sites. The same 2003 report found residents in Annan near Chapelcross would be expected to be subjected to an almost imperceptible annual dose of direct radiation of 110 uSv.

A further survey in 2015 investigated radiation levels in the area and along a pipeline to the estuary. Maximum dosages of 0.0504 μSv/hr above background levels were found at the perimeter of the site. This reduced to 0.0318 μSv/hr at a distance of 300 metres from the power station [28].

6.3.3 Experiment Results

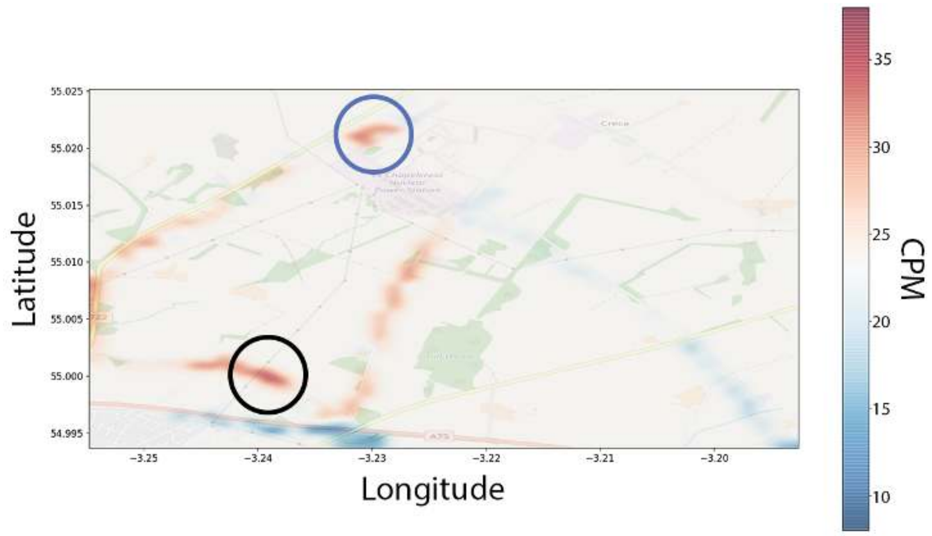

Figure 34: Radiation heat map of the area surrounding Chapelcross decommissioned power station. The area over which measurements were taken was 3km^2, however only 1km^2 is shown for clarity. In black the area of greatest intensity is highlighted. In blue the area in which the rover was deployed is highlighted.

The results from the experiment were processed to form a heat map (Figure 34), an interactive version of the map was simultaneously produced allowing the exact CPM for an area be found using a cross hair cursor. An average CPM of 23 was found by taking the mean of 900 measurements taken in the $3km^2$ area surrounding the power station. The hues and intensities of the colours on the heat map are relative to this average.

6.3.4 Results Discussion

Initially data was recorded with the sensor unit mounted to the exterior of a passenger car. Once in the vicinity of the power station the rover was deployed. The rover was driven along an abandoned airstrip adjacent to the power station at an average velocity of 9 km/h, whilst the operator was stationed at the road side 200 metres away. All navigation was done using the on-board camera viewed via the GUI. At the perimeter fence the average dose rate was found to be 34 CPM (0.194 μSv/hr). This was 11 CPM (0.0627μSv/hr) above the measured background rate for the area, a 22% difference from the value observed in 2015. The rover was then driven to the location 300 metres away from the station previously measured. Here the rover remained stationary for five minutes, an average reading of 27 CPM was recorded over this time.This represented a dose rate of 0.0228μSv/hr above the background rate, a 33% difference from the previously measured value. These values were both significantly different from the previously observed values. One measurement was above the previous recorded data whilst the other was below, this excludes the possibility that the discrepancies were due to a bias. The previous values were recorded in 2015, since then the state of the nuclear site has evolved. Due to the time period between the recordings it was concluded that the 2015 data could not be used to determine accuracy. Instead a more recent dataset would be required (Section 6.4.1).

When travelling in the passenger car a peak in the CPM was observed using the GUI. The area in which this occured is highlighted in black (Figure 34). The GUI allowed this peak to be detected real time and so further analysis was able to be performed on the area (Figure 35).

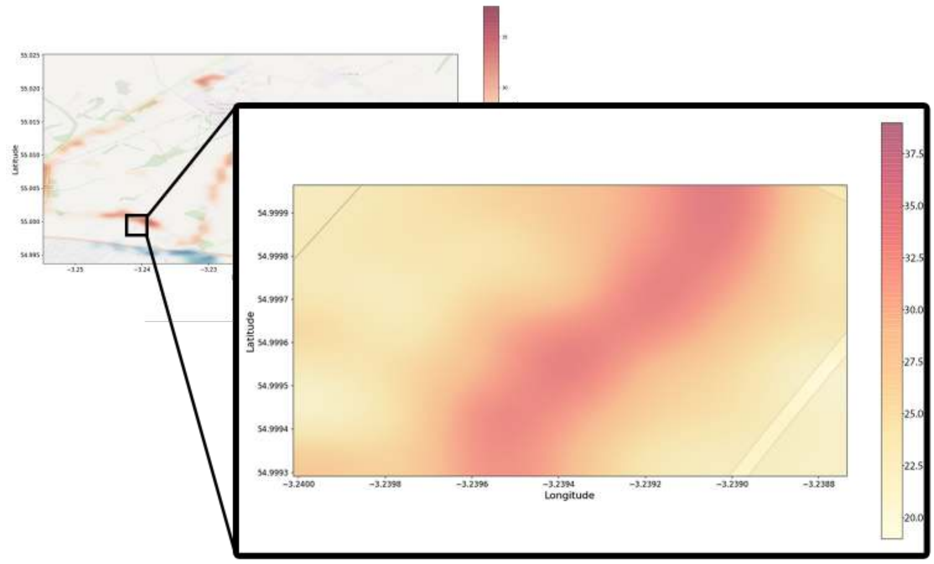

Figure 35: An extensively mapped 3600 m^2 area. Readings were taken every 4 seconds whilst walking in adjacent lines 5 metres apart. Using the GUI a constant line of latitude was followed to ensure a straight path was followed. The data is presented using a continuous colourmap.

This heat map reveals a band of CPM values 35% - 52% higher than the surroundings. It was theorised that this could be due to an underground effluent pipeline, the route of which had not been documented in the 2015 report. A 2002 Radiological Habits Survey gives a cursory look at the route taken by this underground pipe [29]. This report showed the pipeline route coincided with this further analysed area, and so it was concluded that this band of greater dose rate was due to the underground pipeline. Although the 2002 report collected radiation data, the Geiger counter used was only sensitive to gamma radiation so was not directly comparable to data collected by the sensor unit on the rover. However it did show that there was a 60% reduction in the dose rate when moving south from the further analysed site towards the A75/pipeline crossing. This trend was mirrored in our experimentation, the location at which this crossing occured had 72% lower dose rate in our measurements.

6.4 Comparison with bGeigie Nano logging radiation sensor

The bGeigie Nano is an offering from Safecast, a not-for-profit organisation that seeks to map background radiation globally. The bGeigie Nano has similar functionality to the sensor unit created in this project, the company distribute these sensors globally and crowd source maps to document radiation data. The Safecast kit is in use by multiple international organisations, such as the International Atomic Energy Agency, and has undergone calibration tests in multiple research institutes, finding an accuracy of ±10%.

6.4.1 Data comparison

The data from hundreds of bGeigie Nano units is compiled into a single open dataset. The data covers expansive regions of the UK and there was significant overlap between the locations mapped in this project and the location mapped by bGeigie Nano users. Twelve coordinate locations were selected, four from each of the following areas: London, Southampton, and Chapelcross Power Station, and for each of these locations the Safecast radiation data was compared to the data found using the rover.

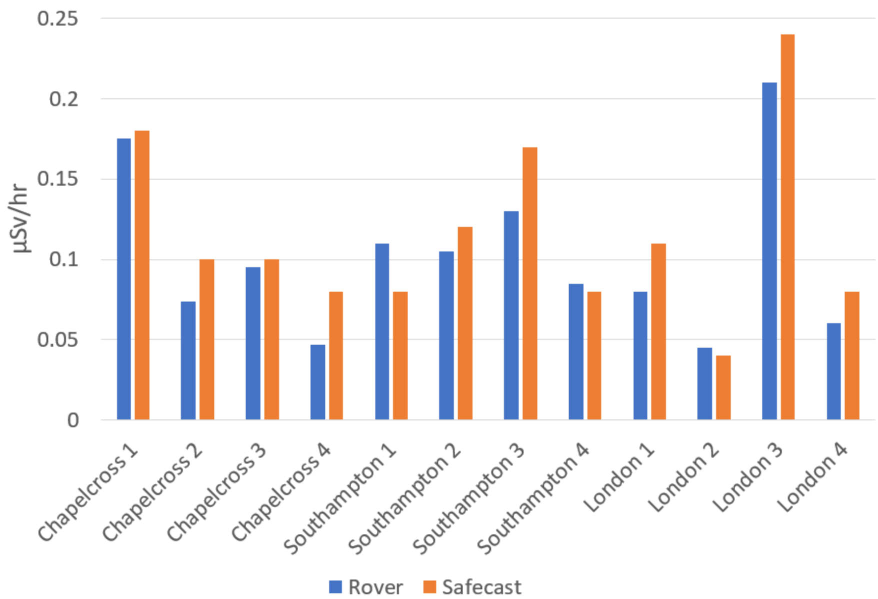

Figure 36: A comparison between the Safecast data and collected data at 12 identical locations spread across three areas.

On average the rover recorded data was 15% below the Safecast data, however there was a close connection between the two data sets, and both showed similar trends. To quantify this correlation a script was written to compare the data collected during this projected to the Safecast data.

Algorithm : Comparing Safecast Data and Collected Data
Step 1: Compile all scraped Safecast data into a CSV in same format as rover data.
Step 2: Compile all collected rover data into single CSV.
Step 3: Round all lat/lon values to 4 dp.
Step 4: Compare the lat/lon values from both csv files using pandas, if they match write to a CSV containing lat, lon, and the recorded radiation data from both devices.
Step 5: Find the differences between radiation values for each matching lat/lon pairing.
Step 6: Using function from scipy library find the Spearman's coefficient.

The most recent UK dataset from Safecast, recorded during the period 09/11/2019 - 03/10/2020, was compared to the 11,204 values recorded during this project. The latitude and longitudes for both datasets were rounded to 4 decimal places, this meant that they would be accurate to within 2 metres. The latitude and longitude values were compared between the datasets and a file of all the matching coordinates, with the associated radiation values were compiled. Statistical analysis was then done to determine the correlation between the data sets and the average percentage difference between the radiation values (Table 2).

Number of UK Safecast data points	181,529
Number of collected data points	11,204
Number of points with matching lat/lon (4 dp)	794
Percentage difference between matching values	-9.6%
Spearman's Rank Correlation Coefficient	0.76

Table 2: Comparison of the data collected by the rover and sensor unit during this project and the Safecast data. Statistical analysis was then performed on data points within two metres to find correlation between the two datasets.

The Spearman's Coefficient of 0.76 indicates a strong correlation (P<0.01) between the two datasets. With the more extensive analysis it was found that the rover data was on average 9.6% below that of the Safecast data. The bGeigie Nano has undergone stringent calibration tests, and so it is reasonable to assume it's data is accurate. Using the dataset as a reference it can be inferred that our data has a good accuracy, however there is a negative bias in our data, indicated by the -9.6% difference.

This negative bias could result from the partial blocking of beta particles by the SBM-20 tube, whereas the pancake tube used in the bGeigie system allows Beta particle detection.

6.4.2 Physical Comparison

The sensor unit created and the bGeigie Nano had similar specifications (Table 3). Primarily the bGeigie Nano acted as a standalone Geiger counter, however the system had GPS and was too able to produce interpolated radiation maps.

	Rover Sensor Unit	**bGeigie Nano**
Controller:	Raspberry Pi 3B+	Arduino Fio
Battery:	5200 mAh	2000 mAh
GPS:	ublox NEO-6M	Adafruit Ultimate GPS
Bluetooth:	Integrated	BLEBee v1 board
Display:	GUI only	GUI + 16-bit OLED
GM Tube:	SBM-20 cylindrical	LND-7317 pancake
Case:	Custom 3D-printed	Pelican 1010
Price:	£166	£600

Table 3: A breakdown and comparison of the components in the rover sensor unit and the bGeigie Nano.

This project aimed to keep costs to a minimum, as a result lower cost, widely available components were chosen (Table 4). This did not come at the cost of functionality and each component was tested to ensure it performed at an acceptable level.

Component	**Cost**
Raspberry Pi 3B+	£35
Geiger Counter	£99
Battery	£18
GPS Module	£14
Total	**£166**

Table 4: A cost breakdown of the components used in the sensor unit. A cheaper battery was substituted as it needed only to power the sensor unit.

The price of our unit was 28% the cost of the bGeigie Nano. Whilst the low cost components are a big driver behind these savings, the lack of accreditation will also contribute to the lower costs. The calibration process undertaken for the bGeigie Nano means that it is accurately able to detect radiation levels. Whereas the measurements taken by our unit serve more to indicate areas of higher radiation than to measure the exact radiation dose rate.

7 Future Work

Alternative Sensors

The code written allowed the Geiger counter to be easily replaced by alternative serial interfacing sensors. When using alternative sensors the collected data would still be automatically georeferenced. This enabled visualisations to be created displaying different characteristics of an area. With the addition of an optical methane sensor portions of gas pipeline could be mapped. Analysing the created heat maps would reveal areas of elevated methane levels indicating the presence of a gas leak. A moisture sensor connected to an actuator would allow monitoring of soil water levels over large agricultural areas. Heat maps showing the saturation levels could then be used to determine the best placement of crops. Alternatively the sensor unit could be mounted on a different transportation platform such as a drone. This would allow inaccessible areas such as bodies of water or mountainous regions to be analysed.

Automated GPS Waypoint Navigation

Currently an operator has to have active control over the rover. Implementing automated GPS waypoint navigation would allow navigation of the rover to a selected GPS location without additional operator input. This would facilitate the rover following a predetermined path with the potential to produce fully featured heat maps, akin to the heat map produced in Figure 35. This would require a more sophisticated object avoidance system, and a vision processing system to analyse the terrain so was far beyond the scope of this project.

Distributed Data Collection

Widescale distribution of the sensor unit would allow more extensive collection of radiation data. A program would then be used to combine the collected data together into a single interactive map. The rover and sensor unit were designed to be inexpensive and open-source. Given this people around the world could build their own sensor units providing a global basis to create additional heat maps.

8 Conclusion

In this project two devices were designed, built, and tested: a remote control rover-style device, and a georeferenced radiation logger. Both devices featured a collection of low-cost components which were tested to assess their reliability, accuracy, and suitability for use. Software solutions were implemented to allow these low-cost components to serve in the place of conventionally more expensive components. This resulted in the combined cost for both devices to be £281 (Appendix A) far below the £350 aim for the project.

The largely 3D printed rover was used in real world conditions, evaluating radiation in multiple locations including a decommissioned nuclear power station. The operator was able to use a Bluetooth controller to direct the rover at distances exceeding 300 metres. This was possible due to the development of a GUI with an integrated video feed, and the transmission of the controller input over 4G using a Raspberry Pi Zero. Subsequent software optimisations were then implemented reducing the video and controller latency to 114 ms which proved to be imperceptible.

The sensor unit was able to log the position of radiation data within 8 metres of the its true location 95% of the time. With the lack of a dosimeter the accuracy of the Geiger counter was unable to be determined directly. However, comparisons with a similar commercial offering revealed a strong correlation ($\rho = 0.76$) when 794 collected data points were analysed. The precision was determined to be $\pm 7.3\%$ of the recorded dose rate. This data was then used to create visual data plots in the form of heat maps. Further, more detailed interactive maps were then generated to give a more discernible look at the collected radiation data.

The project followed an open source methodology, given this it is hoped that others can use what has been learnt to create their own georeferenced radiation logging equipment, or modify the designed system to collect and map other georeferenced data.

References

[1] S. G. Hirschberg S. and D. R, "Severe accidents in the energy sector," Paul Scherrer Institut, 1998.

[2] A. Shlyakhter and R. Wilson, "Chernobyl: the inevitable results of secrecy," *Public Understanding of Science*, vol. 1, no. 3, pp. 251–259, 1992.

[3] Y. Rojavin, "Civilian nuclear incidents: An overview of historical, medical, and scientific aspects." *Journal of emergencies, trauma, and shock*, vol. 4, no. 2, pp. 260–272, 2011.

[4] National Research Council, *Virtual Reality: Scientific and Technological Challenges*, 1st ed. Washington, D.C.: National Academy Press, 1995.

[5] NDT Resource Centre, "Radioactive decay," Available at https://www.nde-ed.org/EducationResources/HighSchool/Radiography/radioactivedecay.htm, [Accessed 15th Nov 2020].

[6] Socratic, "Gamma radiation," Available at https://socratic.org/questions/why-is-gamma-decay-more-dangerous-than-alpha-decay-or-beta-decay, [Accessed 28th Nov 2020].

[7] C. Woodford, "Geiger counters," Available at https://www.explainthatstuff.com/how-geiger-counters-work.html, [Accessed 23rd Nov 2020].

[8] U.S. Environmental Protection Agency , "Epa radiogenic cancer risk models and projections for the u.s. population," 2011.

[9] C. Woodford, "Geiger counters," Available at https://www.explainthatstuff.com/how-geiger-counters-work.html, [Accessed 24th Nov 2020].

[10] US Department of Health, "Personal protective equipment (ppe) in a radiation emergency," Available at https://www.remm.nlm.gov/radiation_ppe.htm, [Accessed 23rd Nov 2020].

[11] G. H. Günter Niemeyer, Carsten Preusche, *Springer Handbook of Robotics*, 1st ed. Berlin, Heidelberg: Springer, 2008.

[12] M.-J. Kraak and F. Ormeling, *Cartography: Visualization of Geospatial Data*, 3rd ed. Essex, United Kingdom: Pearson Education, 2010.

[13] L. Griffiths, "Driving part optimisation," *tct Magazine*, 2017, [Accessed 27th Feb 2021]. [Online]. Available: https://www.tctmagazine.com/additive-manufacturing-3d-printing-news/driving-part-optimisation/

[14] Raspberry Pi Foundatian, "Raspberry pi power supply," Available at https://www.raspberrypi.org/documentation/hardware/raspberrypi/power/README.md, [Accessed 10th Jan 2021].

[15] J. Keyzer, "Geiger counter parts," 2011, [Accessed 18th Apr 2021]. [Online]. Available: https://mightyohm.com/blog/products/geiger-counter/

[16] gstube, "Sbm-20 parameters and characteristics," 2007, [Accessed 10th Mar 2021]. [Online]. Available: https://www.gstube.com/data/2398/

[17] M. Manohar, "Controlling servo motor with a potentiometer!" 2017, [Accessed 18th Apr 2021]. [Online]. Available: https://miymakers.wordpress.com/2017/05/12/controlling-servo-motor-with-a-potentiometer/

[18] MIT Nuclear Engineering Department, "Build your own geiger-müller counter," 2015.

[19] M. Donya, M. Radford, A. ElGuindy, D. Firmin, and M. H. Yacoub, "Radiation in medicine: Origins, risks and aspirations," *Global Cardiology Science and Practice*, vol. 2014, no. 4, 2015.

[20] US Nuclear Regulatory Commission, "Natural background sources," Available at https://www.nrc.gov/about-nrc/radiation/around-us/sources/nat-bg-sources.html, [Accessed 17th Dec 2020].

[21] Argonne National Laboratory, "Natural decay series: Uranium, radium, and thorium," 2005.

[22] A. Eštoková and L. Palaščáková, "Assessment of natural radioactivity levels of cements and cement composites in the slovak republic," *International Journal of Environmental Research and Public Health*, vol. 10, no. 12, pp. 7165–7179, 2013.

[23] C. Nuccetelli, R. Rusconi, and M. Forte, "Radioactivity in drinking water: Regulations, monitoring results and radiation protection issues," *Annali dell'Istituto superiore di sanita*, vol. 48, pp. 362–373, 12 2012.

[24] M. Donya, M. Radford, A. Elguindy, D. Firmin, and M. Yacoub, "Radiation in medicine: Origins, risks and aspirations," *Global Cardiology Science and Practice*, vol. 2014, 12 2014.

[25] M. Grimston, W. Nuttall, and G. Vaughan, "The siting of uk nuclear reactors," *Journal of radiological protection : official journal of the Society for Radiological Protection*, vol. 34, pp. R1–R24, 04 2014.

[26] National Decommissioning Authority, "One more pond to clean," Available at https://nda.blog.gov.uk/2020/08/10/one-more-pond-to-drain/, 2020, [Accessed 21st Jan 2021].

[27] S. J. Watson, A. L. Jones, W. B. Oatway, and J. S. Hughes, "Ionising radiation exposure of the uk population: 2005 review," *Public Health England*, 2005.

[28] A. Tyler, A. Watterson, and i. Dale, "Radiological habits survey chapelcross 2015 public report," *Scottish Environmental Protection Agency*, 04 2017.

[29] J. R. Tipple, K. A. McTaggart, M. Sherlock, "Radiological habits survey, chapelcross liquid effluent pipeline, 2002," *Scottish Environment Protection Agency*, 2002.

9 Appendix

9.1 Appendix A: Costing

Component	Cost
Sensor Components	
Raspberry Pi 3B+	£35
Geiger Counter	£99
GPS Module	£14
Subtotal	**£148**
Rover Components	
Plastic Filament	£38
Suspension Struts	£12
Servo Motor	£6
Brushless Motor	£25
ESC	£30
Pi Zero W	£5
Buck Converter	£7
Additional Hardware	£10
Subtotal	**£133**
Total	**£281**

Table 5: Cost breakdown of the sensor and rover components.